Baseline and Requirements for a Luminosity Monitoring at the LHC

E. Gschwendtner * and **M. Placidi** †

January 5, 2004

1 Introduction

Proton-proton collisions at the high luminosity Interaction Points (IP) of the Large Hadron Collider (LHC) will produce high fluxes of neutrons and photons that will be intercepted by the TAN neutral absorbers [1] located about 140 m downstream the IP1 and IP5 collision points. The energy associated to the showers initiated by the neutral flux from the IPs is proportional to the charge of the colliding bunches and hence to the luminosity.
Detectors suitable for providing information on the shower population with response times compatible with the 40 MHz bunch collision frequency will be installed in instrumental slots machined inside the copper core of the absorbers and will be used to monitor and optimize the LHC luminosity at a bunch-by-bunch rate [2].
The shower development in the TAN absorber material has been simulated using the MARS14 code [3] [4] to assess the required performance of the detectors.
This paper summarizes the simulation studies together with the LHC high luminosity scenarios and accounts for the present status of development of the detectors and their technical performance.

2 Requirements for the LHC Luminosity Monitors

A bunch-by-bunch relative luminosity measurement at the four LHC experiments (ATLAS, ALICE, CMS, and LHC-B) will provide an adequate diagnostic tool for the control of the collision parameters in view of a global optimization of the integrated luminosity performance of the accelerator.
On-line luminosity information with a $\pm 1\%$ accuracy at 10^{34} cm^{-2} s^{-1} design luminosity will be distributed at about 1 Hz rate to each experiment. The machine luminosity detectors will be calibrated against absolute information from the TOTEM [5] monitors in the 10^{28} to 10^{31} cm^{-2}s^{-1} range and from the LHC experiments.
Applications of the on-line luminosity monitoring will include:

- Beam finding procedures;
- Optical tuning of the interaction regions;
- Optimization and control of the bunch overlap;
- Consistency checks of the luminosities at the different interaction points (IP);
- Investigation on possible differences between luminosities at ATLAS (IP1) and CMS (IP5);

*Geneva University and CERN, Geneva, Switzerland
†Present address: LBNL/AFRD, Berkeley, CA 94720, U.S.A.

3 Bunched Beam Luminosity

3.1 Notations

We express the general form for the luminosity produced by multi-bunch beams crossing at a given Interaction Point as the contribution of the **bunch-by-bunch luminosities** $\mathcal{L}_{\rm sb}$:

$$\mathcal{L}(IP_i) = \sum_{b_i=1}^{k_{\rm b}^*} \mathcal{L}_{\rm sb}(b_i) \tag{1}$$

where b_i identifies a particular **pair of bunches** $(1m, 2n)$ in **beam1** and **beam2** colliding at the i^{th} IP and the summation is extended to the **smallest** number $k_{\rm b}^*$ of bunches in either beam.
For Gaussian beam distributions the single-bunch luminosity at the i^{th} IP has the general expression:

$$\mathcal{L}_{\rm sb}(b_i) = f_{\rm rev} \underbrace{\frac{N_{1m}\, N_{2n}}{2\pi\, \Sigma_{{\rm x}i}\, \Sigma_{{\rm y}i}} \cdot F_1(\theta_{\rm i}^*) \cdot F_2(\sigma_{\rm s}, \beta_{{\rm z}i}^*) \cdot F_3(\delta {\rm z}_{i,mn}^*)}_{\mathcal{L}_{{\rm x}i}} \tag{2}$$

where $\mathcal{L}_{{\rm x}i}$ is the luminosity per bunch crossing, N_{1m}, N_{2n} are the populations of the b_i^{th} pair of colliding bunches and $\Sigma_{{\rm x}i}\, \Sigma_{{\rm y}i}$ their convoluted transverse sizes:

$$\Sigma_{{\rm z}i} = \left[\sqrt{(\sigma_{1{\rm z}}^*)^2 + (\sigma_{2{\rm z}}^*)^2}\right]_{IP_i} = \sqrt{\varepsilon_{1{\rm z}}\, \beta_{1{\rm z}i}^* + \varepsilon_{2{\rm z}}\, \beta_{2{\rm z}i}^*} \qquad ({\rm z=x,y})\ . \tag{3}$$

The reduction factor F_1 [6] for operation with a non-zero crossing angle $\theta_{\rm i}^*$ might differ from one IP to another as deviations from the nominal θ^* value (Table 1) may be required during the tuning of each interaction region. The hourglass factor F_2 involves the bunch-length $\sigma_{\rm s}$ and is typical of each IP via the beta-functions $\beta_{{\rm z}i}^*$. The reduction factor F_3 from non-zero collision offsets between each pair of colliding bunches reads:

$$F_3(\delta {\rm z}_{i,mn}^*) = \exp\left[-\frac{1}{2}\left[\left(\frac{\delta {\rm x}_{i,mn}^*}{\Sigma_{{\rm x}i}}\right)^2 + \left(\frac{\delta {\rm y}_{i,mn}^*}{\Sigma_{{\rm y}i}}\right)^2\right]\right] \tag{4}$$

where the impact parameters $\delta {\rm z}_{i,mn}^* \equiv (\delta {\rm x}_{i,mn}^*, \delta {\rm y}_{i,mn}^*)$ are the centroid offsets of the colliding bunches.

In the most general situation, up to four different emittance and beta values characterize the beam sizes represented by the expression (3) at each IP. The machine luminosity monitors are intended to provide the appropriate tools for the tuning of the optical parameters of each interaction region in order to reproduce the operational conditions for optimum luminosity performance:

$$\varepsilon_{1{\rm z}}\, \beta_{1{\rm z}i}^* = \varepsilon_{2{\rm z}}\, \beta_{2{\rm z}i}^* \quad \rightarrow \quad \sigma_{1{\rm z}}^* = \sigma_{2{\rm z}}^* = \sigma_{{\rm z}i}^* \quad , \quad \Sigma_{{\rm z}i} = \sqrt{2}\, \sigma_{{\rm z}i}^*\ . \tag{5}$$

Under these conditions the impact parameter function (4) takes the form:

$$F_3(\delta {\rm z}_{i,mn}^*) = \exp\left[-\frac{1}{4}\left[\left(\frac{\delta {\rm x}_{i,mn}^*}{\sigma_{{\rm x}i}^*}\right)^2 + \left(\frac{\delta {\rm y}_{i,mn}^*}{\sigma_{{\rm y}i}^*}\right)^2\right]\right] \tag{6}$$

and the equation (1) for the luminosity at the i^{th} IP reads:

$$\mathcal{L}(IP_i) = \underbrace{f_{\rm rev} \sum_{b_i=1}^{k_{\rm b}^*} \frac{\gamma\, N_{1m}\, N_{2n}}{4\pi\, \varepsilon_{\rm n} \sqrt{\beta_{{\rm x}i}^*\, \beta_{{\rm y}i}^*}} \cdot F_1(\theta_{\rm i}^*) \cdot F_2(\sigma_{\rm s}, \beta_{{\rm z}i}^*)}_{\hat{\mathcal{L}}(IP_i)} \cdot \exp\left(-\frac{|\tilde{\mathbf{z}}_{\mathbf{i,mn}}|^2}{4}\right) \tag{7}$$

where $\varepsilon_{\rm n}$ is the normalized emittance and $\tilde{\mathbf{z}}_{\mathbf{i,mn}}$ the bunch-to-bunch collision offsets normalized to the transverse bunch sizes at each IP [7]:

$$\tilde{\mathbf{z}}_{\mathbf{i,mn}} \equiv (\tilde{x}_{i,mn}, \tilde{y}_{i,mn}) = \left(\frac{\delta \mathrm{x}^*_{i,mn}}{\sigma^*_{\mathrm{x}i}}, \frac{\delta \mathrm{y}^*_{i,mn}}{\sigma^*_{\mathrm{y}i}} \right) . \tag{8}$$

The quantity $\hat{\mathcal{L}}(IP_i)$ is the optimum luminosity achievable if the collision offset could be compensated for each pair b_i of colliding bunches.

3.2 Operational considerations

The general expression (7) contains the ingredients characterizing the LHC luminosity performance and justifies the requirements to resolve the bunch-by-bunch luminosity.

Substantial deviations from the design luminosities may actually result even after the optical functions of each ring have been tuned to the design figures. Charge differences in the bunches colliding at a given IP and collision-related features (crossing angle, collision overlap) specific to the orbits of bunches occupying different azimuthal positions in the rings (Pacman bunches) can play a role in this process.

A bunch-by-bunch luminosity monitoring at each IP will then constitute a useful tool for initial beam finding, tuning the luminous regions and eventually optimizing the overall luminosity performance of the accelerator. It will contribute in identifying deviations of the beam parameters from the design specifications, complementing task-oriented beam instrumentation for emittance and orbit quality control.

Feedback-based procedures conceived to control the collision parameters at each IP will eventually constitute, together with a fast and accurate beam orbit monitoring system, the essential tools for any luminosity optimization and improvement process.

3.2.1 The IP1 and IP5 Interaction Points

For symmetry reasons the same pairs of bunches will collide in IP1 and IP5, diametrically located in the accelerator. Their luminosity will not be affected by the actual bunch pattern in the two beams nor by differences in the bunch populations along the beam structures. Possible luminosity discrepancies between IP1 and IP5 will be nonetheless indicative of beam optics mismatches leading to deviations from the design assumptions on the beam sizes in collision expressed by Eq. (5).

3.2.2 Luminosity control in IP2

The impact parameter of Eq. (6) can be controlled to deliberately reduce the luminosity at a given interaction point (e.g. IP2 / *ALICE*) without affecting the other experiments.
The luminosity reduction factor generated by the non-zero collision offset of Eq. (8) is, from Eq. (7):

$$\left[\frac{\mathcal{L}(|\tilde{z}_{i,mn}|)}{\hat{\mathcal{L}}} \right]_{IP_i} \simeq \begin{cases} 0.998 & (|\tilde{\mathbf{z}}_{\mathbf{i,mn}}| = 0.1) \\ 0.94 & (\ \ '' \qquad 0.5) \\ 0.37 & (\ \ '' \qquad 2) \quad \text{(Beam finding)} \\ 0.002 & (\ \ '' \qquad 5) \quad \text{(IP2 / } ALICE\text{)} \end{cases} \tag{9}$$

A reduction factor of the order of $2 \cdot 10^{-3}$ or more in the luminosity at IP2 can be achieved by adopting a dedicated optics with larger beta-functions and/or by properly tuning the local average collision offset.

3.3 Parameters and Operational Scenarios for the LHC

Nominal parameters for proton beams colliding in the high luminosity interaction points IP1 (ATLAS) and IP5 (CMS) are collected in Table 1.

Table 1: *LHC design beam parameters at IP1 and IP5.*

Parameter		**Nominal pp Run**	**Unit**
Beam Energy	E	7.0	TeV
Lorentz factor	γ	7.46×10^3	
Revolution frequency	$f_{\rm rev}$	11.2455	kHz
RF frequency	f_{RF}	400.790	MHz
Collision frequency	$f_{\rm x}$	40.790	MHz
Bunch spacing	$\tau_{\rm b}$	7.485 | 24.951	m | ns
Colliding bunches/beam	$k_{\rm b}$	2808	
Normalized emittance	$\varepsilon_{\rm n}$	3.75	μm rad
IP β-value	$\beta^*_{\rm x}$, $\beta^*_{\rm y}$	0.50	m
Bunch transverse sizes (rms)	$\sigma^*_{\rm x}$, $\sigma^*_{\rm y}$	15.9	μm
Bunch divergence (rms)	$\sigma'^*_{\rm x}$, $\sigma'^*_{\rm y}$	31.7	μrad
Bunch length (rms)	$\sigma_{\rm s}$	8.4 | 0.280	cm | ns
Number of protons/bunch	N_1, N_2	$1.13 \cdot 10^{11}$	
Total crossing angle	θ^*	300	μrad
Crossing angle form factor	$F(\theta^*)$	0.784	
Luminosity/bunch crossing	$\mathcal{L}_{\rm x}$	$3.2 \cdot 10^{26}$	cm^{-2}
Single-bunch luminosity	$\mathcal{L}_{\rm sb}$	$3.6 \cdot 10^{30}$	cm^{-2}s^{-1}
Nominal luminosity	$\mathcal{L}$	$1.0 \cdot 10^{34}$	cm^{-2}s^{-1}

Operational scenarios for beam finding, single- and multi-bunch collision modes for proton and ion runs are summarized in Table 2.

Table 2: *LHC operational scenarios at IP1 and IP5 from [8]. We assumed head-on collisions in the first three rows for easy comparison with single-bunch commissioning results without crossing angle. The form factor $F(\theta^*)$ from Table 1 is therefore only used in the last row where a nominal 300 μrad total crossing angle is assumed.*

Operation Mode	**Proton Run**			**Pb-ion Run**		
	$k_{\rm b}$	$N_{\rm b}$ (p / bunch)	$\mathcal{L}_{LHC}$ (cm^{-2} s^{-1})	$k_{\rm b}$	$N_{\rm b}$ (ions / bunch	$\mathcal{L}_{LHC}$ (cm^{-2} s^{-1})
Beam finding($\lvert\tilde{z}_{i,mn}\rvert = 2$)	1	$5 \cdot 10^9$	$3.3 \cdot 10^{27}$			
Single-bunch (pilot)	1	$5 \cdot 10^9$	$9 \cdot 10^{27}$			
Single-bunch (nominal)	1	$1.13 \cdot 10^{11}$	$4.5 \cdot 10^{30}$	1	$7.0 \cdot 10^7$	$1.7 \cdot 10^{24}$
Design performance (†)	2808	$1.13 \cdot 10^{11}$	$1.0 \cdot 10^{34}$	592	$7.0 \cdot 10^7$	$0.8 \cdot 10^{27}$

(†) with 300 μrad total crossing angle.

4 The Interaction Regions

A schematic layout of the LHC interaction regions for the collision point IP5 (CMS) is shown in Fig. 1. Bunches in **beam1** and **beam2** are brought in collision either head-on (continuous line) or at an angle $\theta^* = \theta_1^* + \theta_2^*$ (dotted lines) produced with bumps following the separation schemes described in [9]. A non-zero IP offset $z_{\rm os}^*$ is shown for more generality.

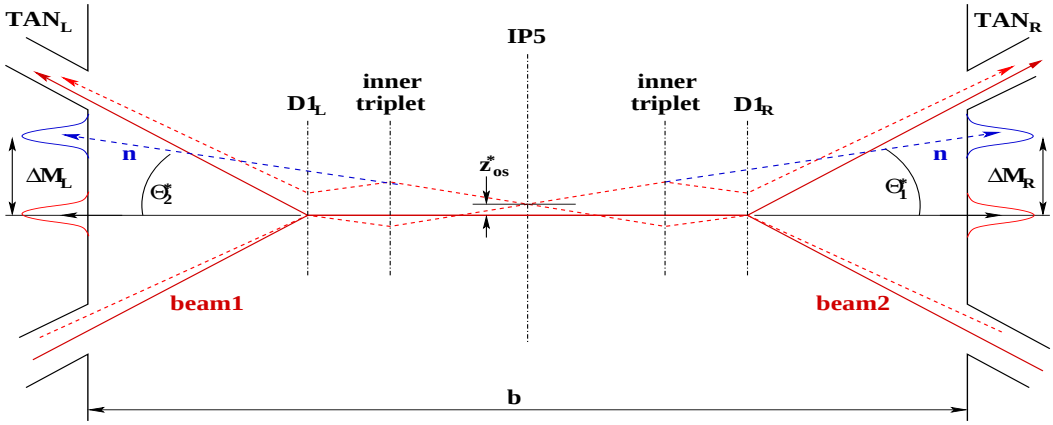

Figure 1: *Schematic layout of the interaction region at IP5 (CMS). A non-zero IP offset $z_{\rm os}^*$ is shown for generality.*

The TAN absorbers at a distance $b/2 = 141.2$ m from IP5 will intercept neutrals produced in the *p-p* interactions. For collision with a horizontal crossing angle $\theta^* = \theta_1^* + \theta_2^*$ the neutral jets will hit the absorbers at positions shifted by $\Delta M_{\rm r}$ and $\Delta M_{\rm l}$ from those associated to head-on collisions. With the nominal crossing angles ($\theta_1^*, \theta_2^* = 150\,\mu$rad) the average shift is $\Delta M_{\rm r,l} \sim 20$ mm.
A measurement of the shift $\Delta M_{\rm r,l}$ in the center-of-gravity of the showers detected at a depth d in the TANs can provide information on the crossing angles:

$$\theta_{1,2}^* = \tan^{-1}\left(\frac{\Delta M_{\rm r,l} - z_{\rm os}^*}{d + b/2}\right) . \tag{10}$$

Neglecting the IP offset $z_{\rm os}^*$, with the assumption that it can be controlled not to exceed a value of $\pm\,0.5$ mm, would yield an error of 2% or less in the evaluation of the collision angles $\theta_{1,2}^*$.

4.1 Collision Modalities

According to the LHC Conceptual Design [10], the crossing angle plane will be **vertical** in IP1 and IP2, and **horizontal** in IP5 and IP8. Nonetheless, as indicated in the Functional Specification Document [8], the sign and the plane of the crossing angle are not frozen to leave more flexibility for the tuning of the IRs optics and of the collision modalities in the early phases of the commissioning.
This requires that the luminosity detectors at the TANs must provide adequate **angular acceptance** to cope with any possible choice of the crossing angle at each IP.

Head-on collisions can be sustained, without parasitic encounters, with up to 145 equidistant bunches in each beam with the IR geometry of Fig. 1. A considerable program of accelerator studies can be performed with more than one bunch per beam before addressing specific studies associated to collisions at an angle.
The associated minimum bunch spacing is $\tau_{\rm b}^* \geq (\overline{\rm D1_L - D1_R}) = 142.714$ m ($\sim 19\,\tau_{\rm b}$, Table 1).

5 Energy deposition in the Neutral Absorbers TAN

Each of the four TAN absorbers installed in the long straight sections LSS1 and LSS5 of the LHC consists of a copper core ($21 \times 26 \times 350\,\mathrm{cm}^3$) which is surrounded by massive steel shielding with a steel/marble albedo trap and incorporates two 5 cm diameter holes for the beam pipes. The power dissipated in the core is about 200 W [11] and is brought primarily by energetic neutrals (45% neutrons and 45% photons) generated at the IP and in materials close to the beam.
Detailed MARS14 Monte Carlo simulations of flux and energy of particles reaching the front face of the IP5 TAN at each *p-p* collision have been performed [12] using DPMJET-3 as an event generator for 14 TeV *p-p* collisions at a 300 μrad total crossing angle.
The neutron and photon fluxes at the TAN surface are shown in Figs. 2 and 3. The ~ 20 mm shift of the neutrons peak is consistent with the IR5 description of Sec. 4 with a horizontal crossing angle. The photons are nearly equally distributed in the region between the two beam-pipes, for they originate not only from the collision point, but also from shower productions in the surrounding materials.

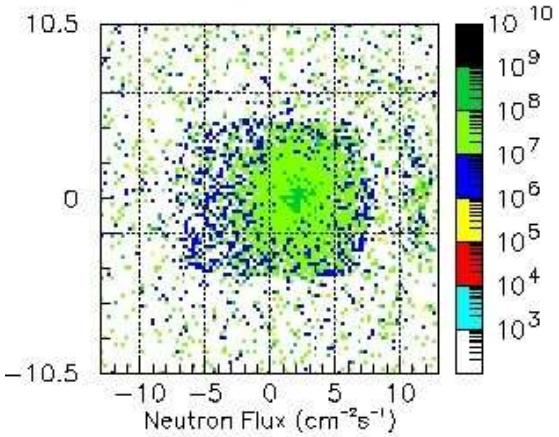

Figure 2: *Neutron flux at the TAN surface.*

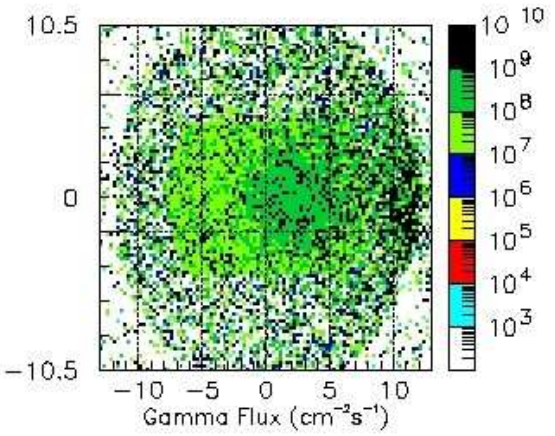

Figure 3: *Photon flux at the TAN surface.*

With a total *p-p* interaction cross-section $\sigma_{\mathrm{pp}} = 80$ mb the number of proton-proton interactions (ppi) per bunch crossing at the design luminosity of $10^{34}\,\mathrm{cm}^{-2}\,\mathrm{s}^{-1}$ is

$$N_{\mathrm{ppi}}(\mathcal{L}) = \sigma_{\mathrm{pp}}\,\mathcal{L}_{\mathrm{xi}} \sim 25\,ppi/\mathrm{Xing} \quad \text{or} \quad 8\cdot 10^8\,ppi/\mathrm{s}\,. \tag{11}$$

Table 3 collects the mean number and energy of particles incident on the TAN absorbers per ppi together with the total particle flux ϕ_{tot} at $8\cdot 10^8$ *ppi*/s.

Table 3: *Average number of particles $\langle N\rangle$, particle energy $\langle E\rangle$ and total energy $\langle N\rangle \times \langle E\rangle$ per ppi incident on the IP5 TAN absorbers [12]. The total particle flux ϕ_{tot} at $8\cdot 10^8$ ppi/s is also shown.*

particle	$\langle N\rangle$	$\langle E\rangle$ [GeV]	$\langle N\rangle \times \langle E\rangle$ [GeV]	ϕ_{tot} [$\mathrm{cm}^{-2}\mathrm{s}^{-1}$]
n	0.479	1516	726	$1.2\cdot 10^6$
γ	301	2.20	662	$6.8\cdot 10^8$
p	0.109	938	102	$2.5\cdot 10^5$
$\pi^{\pm}\,K^{\pm}$	0.875	64.8	56.8	$1.8\cdot 10^6$
$e^{\pm}$	24.5	0.294	7.2	$5.3\cdot 10^7$
$\mu^{\pm}$	0.006	4.87	0.031	$1.4\cdot 10^4$

A neutron flux $\langle N_{\mathrm{n}}\rangle = 0.479\,n/ppi$ with average energy $\langle E_{\mathrm{n}}\rangle$=1.516 TeV and a photon flux $\langle N_{\gamma}\rangle = 301\,\gamma/ppi$ with average energy $\langle E_{\gamma}\rangle$=2.20 GeV will strike the TAN absorbers at each *p-p* collision.

The longitudinal position of the maximum of the electromagnetic shower initiated by a 2 TeV Gaussian neutron beam is about 20 to 30 cm (see Fig. 4). The transversal shower development at different depths is shown in Fig. 5.

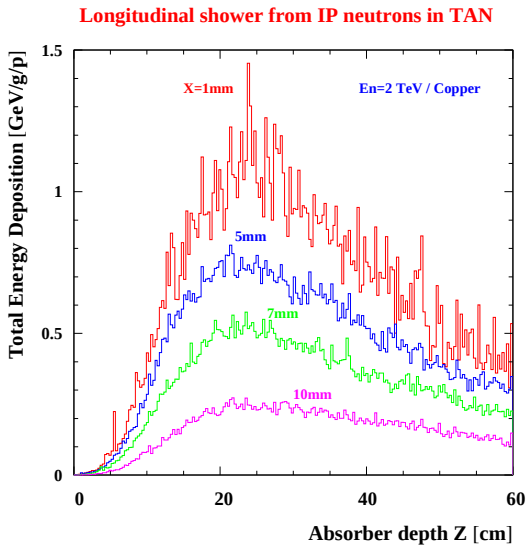

Figure 4: *Longitudinal development of showers initiated in the TAN absorbers by 2 TeV neutrons at different positions X from the beam axis.*

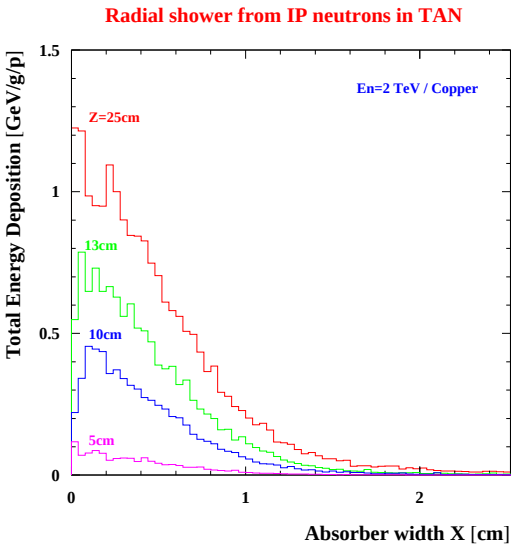

Figure 5: *Transverse distribution of showers initiated in the TAN absorbers by 2 TeV neutrons at different depths Z in the absorber.*

The normalized spatial distributions of the charged component of the shower initiated by 2 TeV neutrons in Copper are shown in Figs. 6 and 7 for two absorber depths. The shift of about 20 mm in the center-of-gravity of the distributions is consistent with the 150 μrad crossing angle used in the simulation.

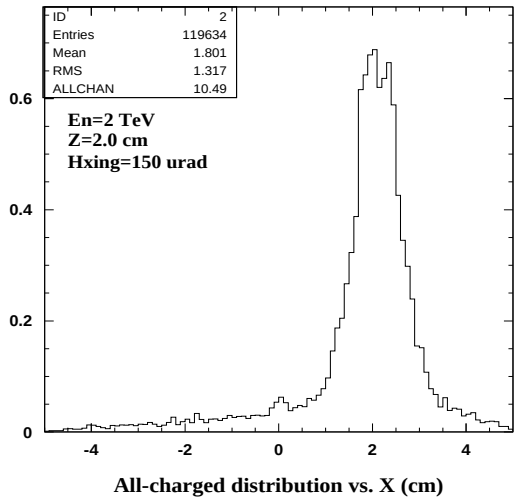

Figure 6: *Normalized distribution of the charged shower component at z=2 cm depth in the TAN absorbers initiated by 2 TeV neutrons. Shown is the number of charged secondaries per incident neutron from pp collisions at 150 μrad crossing angle.*

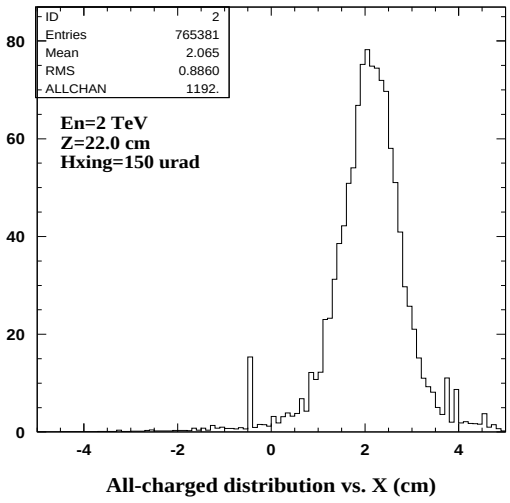

Figure 7: *Normalized distribution of the charged shower component at z=22 cm depth in the TAN absorbers initiated by 2 TeV neutrons. Shown is the number of charged secondaries per incident neutron from pp collisions at 150 μrad crossing angle.*

6 Luminosity Detectors

Detectors suitable to measure the yield of charged particles in the TAN absorbers will be installed in the instrumental slot located between the two beam pipes [1]. A detector with a square cross-section of $94 \times 94\,\mathrm{mm}^2$ is required to cope with the crossing angle considerations of Sec. 4.
In order to calculate the number $N_{\mathrm{abs}}(z, \mathcal{L})$ of charged secondaries at a depth z in the absorber we assume a detector geometric acceptance of $\eta_{\mathrm{det}} \sim$60 % for the flux $\langle N_{\mathrm{n}} \rangle = 0.479\, n/ppi$ of neutrons reaching the TAN at each *p-p* collision (Table 3). With the charged shower multiplicities $M_{\mathrm{ch}}(z)$ integrated from Figs. 6 and 7 we get for the flux of charged secondaries at the absorber depth z:

$$N_{\mathrm{abs}}(z, \mathcal{L}) = \underbrace{\eta_{\mathrm{det}}\, \langle N_{\mathrm{n}} \rangle\, M_{\mathrm{ch}}(z)}_{N_{\mathrm{ch}}(z)} \cdot N_{\mathrm{ppi}}(\mathcal{L})\ . \tag{12}$$

The flux $N_{\mathrm{ch}}(z)$ of charged particles per ppi in the shower is a function of the absorber material and thickness (Fig. 4) and of the energy of the primary neutrons. The term $N_{\mathrm{ppi}}(\mathcal{L})$ provides the dependence on the luminosity via Eq. (11).
Simulated fluxes of charged secondaries at two detector positions z in the TAN are collected in Table 4. The non-linear dependence on the detector position in the absorber of the multiplicities M_{ch} and of the associated charged fluxes N_{ch} is consistent with the shape of the longitudinal shower development shown in Fig. 4. The luminosity-dependent figures in the last column are for a $10^{34}\,\mathrm{cm}^{-2}\mathrm{s}^{-1}$ design performance.

Table 4: *Simulated fluxes of charged secondaries at detectors located at depths z=2 and 22 cm inside the TAN absorbers. The third column gives the charged fluxes normalized to one ppi. The figures in the last column are for a* $10^{34}\ cm^{-2}s^{-1}$ *design luminosity (Eq. 11).*

z (cm)	M_{ch} (charges / n)	N_{ch} (charges / ppi)	N_{abs} (charges / Xing)
2	10.5	**3**	75
22	1192	**345**	8625

6.1 Design Constraints and Technical Approaches

Severe constraints influence the design and the technical choices of the detectors:

- Operation in a high radiation environment. Characteristic figures [1] *per operational year at design luminosity* are:

$$170\,\mathrm{MGy} \quad , \quad 4.6 \cdot 10^{16}\,\mathrm{n/cm}^2 \quad , \quad 4.7 \cdot 10^{15}\,\mathrm{charged\ hadrons/cm}^2; \tag{13}$$

- A bunch-by-bunch (40 MHz) luminosity information;
- A reasonably high signal to noise ratio over a $(10^{24} \div 10^{34})\,\mathrm{cm}^{-2}\mathrm{s}^{-1}$ luminosity range (Table 2).

Two detector capable of meeting these requirements are being considered: **Polycrystalline CdTe** [13] and **Ionization Chambers** [14]. Both technical approaches are described below.

6.2 Polycrystalline CdTe Detectors

Techniques for producing Polycrystalline CdTe detectors with thicknesses between 50 μm and 700 μm and decay times of a few nanoseconds are developed at the LETI laboratories [15].

A minimum ionizing particle (*mip*) creates about 5×10^4 electrons in a 300 μm thick CdTe detector. However, only a fraction of the electrons are collected at the electrodes since the charge carrier lifetime in the polycrystalline material is very low.

CdTe detectors are presently produced at LETI in disks of 1.6 cm diameter and $\sim 380\,\mu$m thickness. Each disk is gold-plated for ground and high voltage connections (Fig. 8). A bias voltage between 200 V and 600 V represents a typical working point.

Figure 8 shows a single detector in its housing as used for the characterization. The Copper-Beryllium spring contact holds the detector and provides both the high voltage and the signal readout.

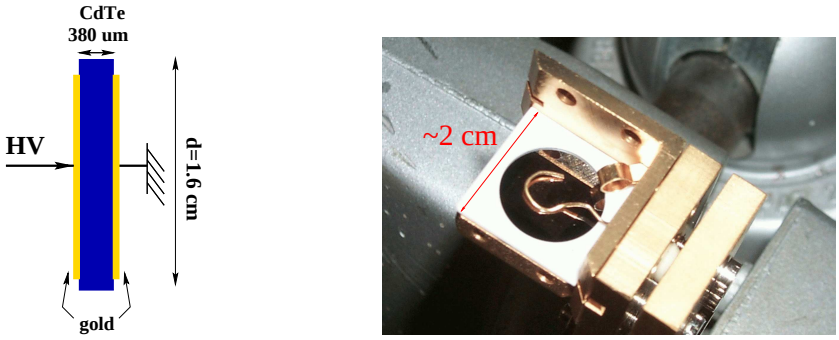

Figure 8: *Geometry and photo of a CdTe element in its housing.*

6.2.1 Detector Properties and Characteristics

The physical properties of different semiconductor materials are collected in Table 5.
The main characteristics of polycrystalline CdTe detectors are:

- A response signal showing a sub-nanosecond rise-time and a FWHM duration of $\sim$5 ns (Fig. 9).
- An intrinsic sensitivity of $\sim 1.7 (\sim 2.3) \times 10^2$ electrons/*mip*/μm at a bias voltage of 400 (600) V.
- A signal to noise ratio (SNR) of about 1 to 2 for one *mip*.
- Temperature tests performed between $40\,^\circ$C and $80\,^\circ$C show a dark current rise from $30\,\mu$A to $420\,\mu$A at 400 V. However, the signal response stays independent of the temperature.
- Radiation tests with neutron fluxes up to 10^{17} n/cm^2 show no significant changes in the carrier life time [16]. The sensitivity and the dark current behavior after irradiation have to be verified.

Table 5: *Physical properties and charge creation per minimum ionizing particle for different semiconductor materials with a thickness of* $300\,\mu$m.

Parameter	**CdTe**	GaAs	Si	Diamond
atomic number	**48-52**	31-33	14	6
density [g/cm^3]	**5.85**	5.32	2.33	3.51
$(dE/dx)_{min}$ [MeV/g/cm^2]	**1.26**	1.4	1.66	1.78
Ionization potential [eV]	**4.43**	4.2	3.61	13
Number of charges/*mip*	**50000**	53000	32200	11850

A detector prototype, schematically shown in Fig. 10, has been built at the LETI laboratories and is being tested at LBNL. It consists of two arrays of five CdTe disks with a thickness of 400 μm, a diameter of 16 mm and an active area of $\sim$110 mm^2. The overall size fits into the detector slot in the TAN.

Given their high sensitivity the CdTe detectors could be installed inside the TAN at depths of about 2 to 5 cm, where the shower is far from its maximum (Fig. 4) and the radiation hardness requirements could be relaxed. A deeper positioning inside the TAN might nevertheless be required to attenuate the contribution from the photons (Sec. 5).

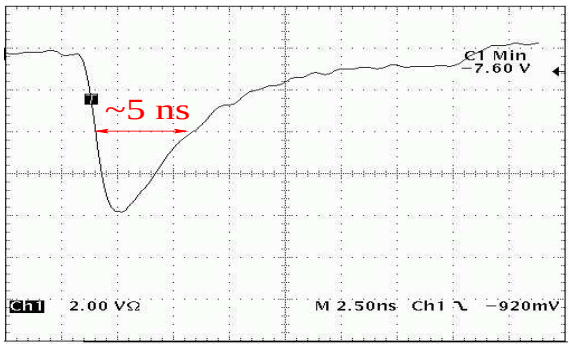

Figure 9: *Typical single CdTe detector response to a picosecond laser pulse.*

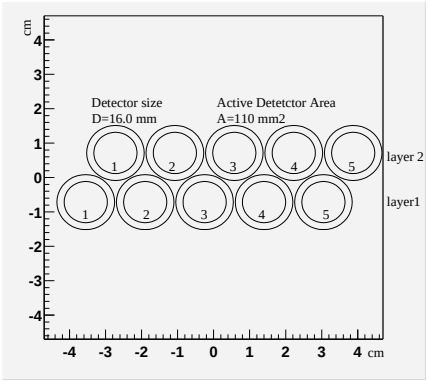

Figure 10: *Sketch of the CdTe array detector prototype for beam tests. Each of the ten elements is 16 mm in diameter and has a 110 mm^2 active area.*

The charged multiplicity for a detector situated 5 cm inside the TAN is estimated from the number of particles hitting the absorber (Figs. 2 and 3) and their induced shower particles at the detector location. With the proposed assembly about 30 charged particles per ppi hit each CdTe detector button, giving a SNR of ∼30. At the shower maximum the multiplicity is higher and about 140 charged particles per ppi would hit a detector element [17].

6.3 Ionization Chamber

The Ionization Chamber detectors are being designed and built at LBNL with the collaboration of the INFN section of the Pavia University. They are supposed to be installed in the instrumental slot of the TAN absorbers at a depth consistent with the shower maximum (about 25 cm of copper, see Fig. 4).
A detector prototype was tested on the 300 GeV H4 proton beam at CERN in July 2001. Two quadrants of the Ionization Chamber are shown in Fig. 11 and its main parameters are collected in Table 6.
The performance of the detector and of the associated electronics are reported in Ref. [18] and [19].

6.3.1 Preliminary Performance Results

The chamber was pressurized with four to six atmospheres of a gas mixture of $Ar + N_2(4\%)$ and segmented into four $40 \times 40\,mm^2$ quadrants consisting of 60 gaps (0.5 mm) separated by 1 mm thick Cu plates. The gap width was determined by the requirement for the drift time of the ionizing electrons to be shorter than the 25 ns bunch spacing in the LHC. Six groups of ten plates in parallel were serial connected in each quadrant. The serial-parallel configuration was designed to produce a capacitance of ∼50 pF, chosen by SNR considerations.
A typical waveform of signals obtained at maximum energy deposition of showers initiated by 300 GeV protons at the CERN H4 test beam is shown in Fig. 12. The ∼17 ns signal peaking time is shorter than the bunch separation and allows a deconvolution of successive detector pulses for a bunch-by-bunch luminosity detection at 40 MHz [20].
Data taken while positioning the detector across the incoming beam indicate that information on the transverse position of the shower and hence on the amplitude of the crossing angle can be retrieved from difference-to-sum normalization of the signals from each quadrant.

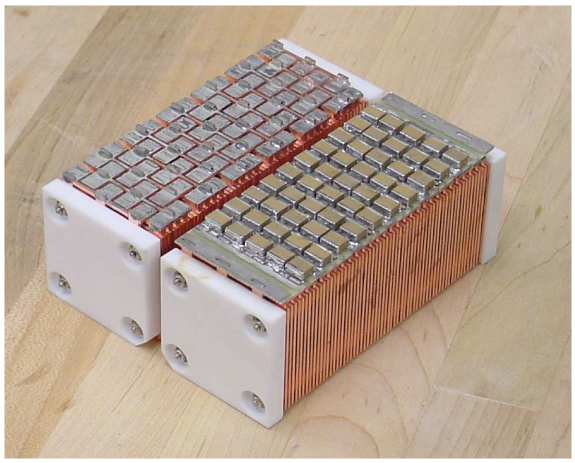

Figure 11: *Photograph of two quadrants of the Ionization Chamber prototype tested on the H4 proton beam at CERN in 2001. Each quadrant provides an active area of* $40 \times 40\ mm^2$.

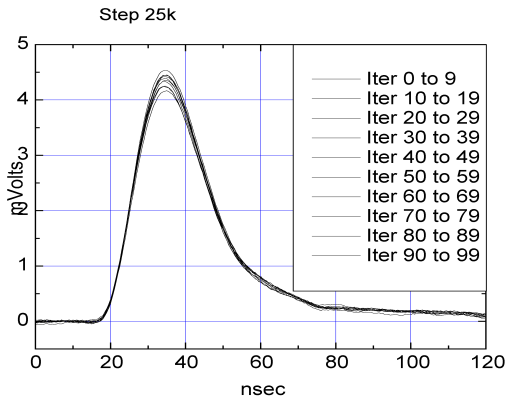

Figure 12: *Signal waveform from the detection of charged secondaries at the shower maximum initiated by 300 GeV protons in iron. Shown is the overlay of ten mean waveforms, each of them associated to 2400 proton showers. The signal peaking time is* $\sim$*17 ns.*

Table 6: *Parameters of the LBNL Ionization Chamber detector (2001 version).*

Parameter	**Value**
Gap width	0.5 mm
Quadrant active area	$40 \times 40\ \mathrm{mm}^2$
No. of gaps	60 (10 parallel $\times$ 6 series)
Gap capacitance	28.3 pF
Gas composition/pressure	Ar+N_2 (1%) / 4 Atm
Gap voltage	150 V
Gap electron transit time	21.7 ns
No. of *p-p* interaction (*ppi*)	25 *ppi*/Xing @ $\mathcal{L} = 10^{34}$
No. of *mips* / *ppi*	268
No. of *mips* / Xing	6.7×10^3 @ $\mathcal{L} = 10^{34}$
No. of ionizing e^- / Xing	10^5/gap

A new version of the detector has been produced at LBNL and is presently being tested with beam to assess its requirements in terms of speed and sensitivity.

7 Outlook

The measurement of the luminosity at a bunch-by-bunch time scale at the four interaction points of the LHC is required to resolve deviations from the design goals and to provide tools for the optimization of the long term performance of the accelerator.

Technical solutions for detectors capable to meet the specifications in terms of rapidity and sensitivity have been identified and prototypes have been developed.

A campaign of beam tests is presently being carried on for both detectors to characterize their performance and assess their radiation resistance.

These informations will guide the technical choices for the construction of the machine luminosity instrumentation for the four interaction regions of the LHC.

References

[1] E. H. Hoyer, N. V. Mokhov and W.C. Turner, *Absorbers for the High Luminosity Insertions of the LHC*, Proc. EPAC98, 22-26 June 1998.

[2] W. C. Turner, *Instrumentation for the Absorbers in the low β^* Insertions of the LHC*, LBNL-42180, August 1998.

[3] N. V. Mokhov, *The MARS Code System User's Guide*, Fermilab-FN-628 (1995).

[4] N. V. Mokhov and O. E. Krivosheev, *MARS Code Status*, Fermilab-Conf-00/181 (2000).

[5] *Total Cross Section, Elastic Scattering and Diffraction Dissociation at the LHC*, The TOTEM Collaboration, CERN/LHCC 99-7, 15 March, 1999.

[6] B. Muratori *Luminosity Considerations for the LHC,* LHC Project Note 301, Sept.11, 2002.

[7] M. Placidi and J. Wenninger, *Interaction Region Diagnostics in* e^+e^- *Ring Colliders*, Proc. Adv. ICFA Beam Dynamics Workshop on Beam Dynamic Issues for e^+e^- Factories, Frascati, Italy, Oct.20-25, 1997.

[8] *Measurement of the Relative Luminosity at the LHC*, Functional Specifi cation LHC-B-ES-0004 rev. 2.0, EDMS Document No.328136, June 20, 2003.

[9] O. Bruning and W. Herr, *A beam separation and collision scheme for IP1 and IP5 at the LHC for optics version 6.1*, LHC Project Report 315, Nov.10, 1999.

[10] *The Large Hadron Collider Conceptual Design*, CERN/AC95-05 (LHC), Oct.20, 1995.
Revised in $http://wwwlhc01.cern.ch:8050/lhc\_proj/owa/lhcp.page?p\_number = 1000$.

[11] N. V. Mokhov and I. L. Rakhno, *Protecting LHC Components against Radiation Resulting from Colliding Beam Interactions*, Fermilab-Conf-01/131 (2001).

[12] N. V. Mokhov *et al.*, *Protecting LHC IP1/IP5 Components Against Radiation Resulting from Colliding Beam Interactions*, Fermilab-FN-732, April 2003.

[13] E. Rossa *et al.*, *Fast Polycrystalline-CdTe Detectors for LHC Luminosity Measurements*, Proc. IEEE Nuclear Science Symposium, San Diego, CA, 4-10 Nov., 2001.

[14] W. C. Turner *et al.*, *Development of a detector for bunch by bunch measurement and optimization of Luminosity in the LHC,* Proc. 8^{th} Pisa meeting on Advanced Detectors, La Biodola, Isola d'Elba, Italy.
NIM **A** 461 (2001) 107-110.

[15] LETI (Laboratoire d'Electronique, de Technologie et d'Instrumentation), CEA/Grenoble, 17 Rue des Martyrs, F38054 Grenoble Cedex, France.

[16] E. Gschwendtner, M. Placidi and H. Schmickler, *Polycrystalline CdTe Detectors: A Luminosity Monitor for the LHC,* Proc. 8^{th} Topical Seminar on Innovative Particle and Radiation Detectors, Siena, Italy, 21-24 Oct., 2002. Nuclear Physics B (Proc. Suppl.) 125 (2003), Sept. 2003.

[17] N. V. Mokhov, *Contribution to the* LHC Luminosity Instrumentation Review, 28 Jan. 2003.

[18] P. S. Datte *et al.*, *Initial Test Results of an Ionization Chamber Shower Detector for a LHC Luminosity Monitor*, IEEE Transactions on Nuclear Science, Vol.50, No.2, April 2003.

[19] P. F. Manfredi *et al.*, *The LHC beam luminosity monitor: accurate charge measurements at 40 MHz repetition rate*, Proc. Elba Conference "Frontier Detectors for Frontier Physics", La Biodola, Isola d'Elba, Italy, May 25-31, 2003. Accepted for publication in Nuclear Instruments and Methods **A**.

[20] W. C. Turner, *Development of a 40 MHz Gas Ionization Chamber for Optimization of LHC Luminosity*. Paper in preparation.